Analytical model of the modulated photoluminescence in semiconductor materials

Nicolas Moron, Baptiste Bérenguier, José Alvarez, Jean-Paul Kleider

Analytical model of the modulated photoluminescence in semiconductor materials

Nicolas Moron[1,2,3], Baptiste Bérenguier[3,4], José Alvarez[1,2,3],
Jean-Paul Kleider[1,2,3]

July 19, 2021

[1] Université Paris-Saclay, CentraleSupélec, CNRS, Laboratoire de Génie Electrique et Electronique de Paris, 91192, Gif-sur-Yvette, France

[2] Sorbonne Université, CNRS, Laboratoire de Génie Electrique et Electronique de Paris, 75252, Paris, France

[3] Institut Photovoltaïque d'Ile de France, 30 Route Départementale 128, 91120, Palaiseau, France

[4] UMR IPVF 9006, CNRS, Ecole Polytechnique Institut Polytechnique de Paris, PSL Chimie ParisTech, IPVF SAS, 91120 Palaiseau, France

Abstract

Modulated photoluminescence (MPL) is an optoelectronic characterization technique of semiconductor materials. Going to high frequencies enables one to characterize fast phenomena, and so materials with a short lifetime such as chalcogenides or III-V absorbers. Some typical signatures have already been experimentally observed. However, physical mechanisms and quantitative analyses are not well understood yet. Here, using both an analytical approach and a full numerical modeling, we study how the energy position of a defect level, its electron and hole capture cross sections, its density, influence the frequency dependence of the MPL phase. We show that quantitative information can be extracted. We also study the effect of additional surface recombination, and of non homogeneities created by carrier generation profiles or asymmetric top surface and bottom surface recombination velocities, where diffusion of the carriers plays a role and can be limiting at high frequency. Finally we apply our model to an experimental result to extract defect parameters of the sample. Our analysis highlights the usefulness of MPL and the importance of having a proper modeling of the experiment.

Keywords : MPL, photoluminescence, modeling, semiconductors

I   Introduction

Photoluminescence (PL) is a proven technique to study semiconductors. As it is contactless and purely optical, it is very useful for the development of applications like LEDs and photovoltaics because experiments can be performed at every stage of the production process (from the raw material to the device) without the need of electrical connections. Photoluminescence is based on radiative recombinations, and one can analyze its spectrum and its intensity. It can be done under steady-state conditions [1][2] or with time-varying excitation. The most famous time-varying mode is the response to a light pulse, leading to transient or time-resolved photoluminescence (TRPL).[3][4]

In modulated photoluminescence (MPL), the sample is sinusoidally illuminated, and we focus on the resulting periodic response of the photoluminescence. The technique has been used to investigate silicon under a small-signal approach in order to measure the differential minority carrier lifetime, with frequencies up to some kHz [5][6][7], but also other materials in the infrared range [8]. It was also recently used on quantum well InGaN LEDs by Reklaitis et al, with frequencies up to 100 MHz [9][10]. A newly developed method in MPL techniques is based on the simultaneous use of two modulating frequencies, to make heterodyne detection and observe non-linearities in high injection rate. In [11] and [12], the authors develop some analytical model to be able to interpret the results by computing the different parameters of the recombination paths. In our experiment and analysis, we use only
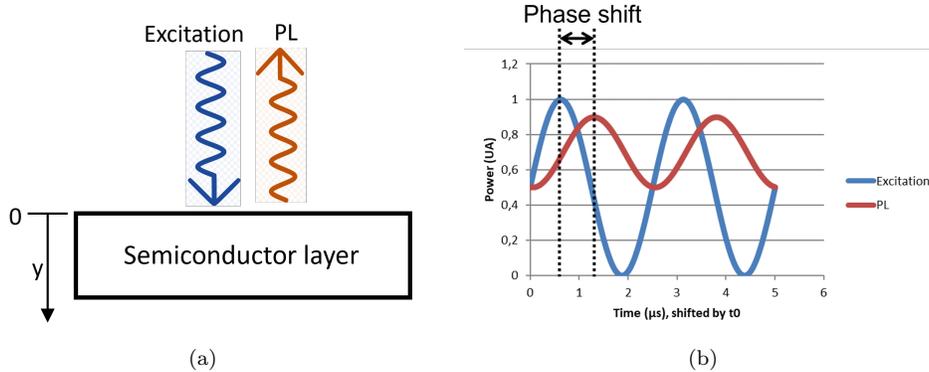
Figure 1: Sketch of the considered structure (a) and principle of MPL (b)

one excitation frequency and a large modulation depth (more than 50%) and frequencies up to 100 MHz. This enables the extension of the technique to semiconductors with short lifetimes, used in thin-film photovoltaic cells for instance, such as CIGS or III-V materials. MPL is, therefore, a new tool of advanced characterization, useful to check the quality of a material or to have a better knowledge of the material, and then to enhance the process of fabrication.

There have already been some works on MPL at high frequency (HFMPL) by Berenguier et al., who have published two articles. In the first one[13], one can see details on the experimental setup, experimental data obtained on a CIGS absorber, and simulation-based analysis. In particular, it shows that the frequency dependence of the MPL phase can exhibit different behaviours : either a monotonous decrease or a local minimum described as (and denoted in the following) a V-shape. We can note that Mickevicius et al. have also observe V-shapes on GaN at low-temperature.[14] In the second one[15], the authors have used simulations to show the impact of the illumination power on the phase diagram, and so the usefulness of doing the characterization at several powers in order to detect specific signatures of defects. Particularly, it offers promising results about detecting shallow traps compared to more well-established techniques such as TRPL.

In this work, we develop an analytical model and use complementary 2D finite-elements simulations to explore to which extent HFMPL can offer a quantitative assessment of defect parameters and of the impact of surface recombination velocity (SRV).

We consider a simple structure with a semiconductor thin layer illuminated from the top surface, as shown in figure 1a. When the periodic excitation is switched on, the time dependence of the photoluminescence signal first exhibits a transient phase corresponding to the onset regime until a periodic quasi-steady-state regime is reached. The periodic PL may not be a perfect sinusoid due to nonlinearities, even in low-illumination conditions. However, we can extract the amplitude and the phase shift between the excitation and the PL signal at the working frequency (called fundamental), as illustrated in figure 1b (t0 being the settling time so that only the steady-state part is shown). The measurements can be repeated at different frequencies, which allows one to plot the phase shift as a function of frequency. This is also called a Bode phase plot (in the following, we will use more simply phase plot), and it is a standard tool in control theory. [16] We can also study the frequency dependence of the amplitude of the modulated part of the photoluminescence, but it contains the same information as the phase plot, and is visually less clear.

In Section II, we lay the theoretical foundations of the analytical model and establish the equations to calculate the phase plot, with a focus on low-illumination conditions. We study the effect of a defect level in the bandgap and show that the phase plot can be very different depending on the energy position of the level. More specifically, we demonstrate the existence of a V-shape in the phase plot when the defect acts as a minority-carrier trap, with its energy close to the minority-carrier band. In Section III, we propose a complementary full numerical simulation, that allows us to validate the analytical model of Section II and to extend the calculations beyond the simplifying assumptions of the analytical model. In particular, in Section III.3 we study the impact of the surface recombination velocity in different cases. Finally, in part IV, we will illustrate the application of our analysis on an experimental result.

2

II Analytical approach

II.1 Phase-shift of the PL

In order not to burden the writing of the equations, we will consider a p-type semiconductor characterized by a concentration of acceptor type dopants, N_a, and with only one level of defects (that we will consider of acceptor type) in the gap at the energy E_t and with a concentration N_t. The following relations can be extended to the case of an n-type semiconductor (by introducing a concentration of dopants of donor type, N_d) and to the case of a donor-type defect level or to several levels of defects. We denote n and p the concentrations of electrons (minority carriers) and holes (majority carriers), and n_t the concentration of defects occupied by an electron.

In order to make the analytical calculation possible, we assume that there is no space dependence of the physical quantities (thus no gradient) and, in particular, the generation rate and carrier concentrations are constant. While this assumption may appear as a crude one, we can note that rather homogeneous carrier concentrations in an illuminated semiconductor can be obtained in AC condition if the homogenization through diffusion is fast compared to the characteristic time scale of the AC signal, i.e. the period of the signal. In addition, we will show in the next section, from full numerical modeling, where we can consider realistic carrier generation profiles and surface recombination velocities, that the main results on the phase plot obtained in this section still remain valid.

The charge neutrality can be written :

$$p = N_a + n + n_t, \tag{1}$$

and the continuity equations for holes and electrons :

$$\frac{dp}{dt} = G - \frac{p}{\tau_{c,h}} + \frac{N_t - n_t}{\tau_{r,h}} - \frac{n}{\tau_{rad}}, \tag{2}$$

$$\frac{dn}{dt} = G - \frac{n}{\tau_{c,e}} + \frac{n_t}{\tau_{r,e}} - \frac{n}{\tau_{rad}}, \tag{3}$$

where G is the photogeneration rate of electron-hole pairs, and the various time constants are defined as:

- for the recombination process characterized by a radiative recombination constant B,

$$\tau_{rad}^{-1} = \omega_{rad} = B.p, \tag{4}$$

- for the capture of electrons by the defect :

$$\tau_{c,e}^{-1} = \omega_{c,e} = v_{th}\sigma_n(N_t - n_t), \tag{5}$$

where σ_n is the electron capture cross-section and v_{th} the thermal velocity (taken identical for electrons and holes),

- for the release of electrons by the defect (de-trapping) :

$$\tau_{r,e}^{-1} = \omega_{r,e} = v_{th}\sigma_n n_i \ \exp(\frac{E_t - E_i}{k_B T}), \tag{6}$$

n_i being the intrinsic carrier concentration, and E_i the intrinsic Fermi level,

- for the capture of holes by the defect :

$$\tau_{c,h}^{-1} = \omega_{c,h} = v_{th}\sigma_p n_t, \tag{7}$$

where σ_p is the hole capture cross-section

- for the release of holes by the defect :

$$\tau_{r,h}^{-1} = \omega_{r,h} = v_{th}\sigma_p n_i \ \exp(-\frac{E_t - E_i}{k_B T}). \tag{8}$$

Note that we have assumed Auger recombination to be negligible since we will not consider very high excitation levels.

The generation rate can be written :

$$G = G_0 + G_1 \sin(\omega t). \tag{9}$$

with $\omega = 2\pi f$ the angular modulation frequency, f the frequency, G_0 the mean value of the photogeneration rate, and G_1 the amplitude of the modulated part.

We remark that some of these time constants are dependent on n_t or p, which are time-dependent, and so they are not really constant, especially when n_t has large variations (we will see that in low-frequency).

In quasi-steady-state, under sinusoidal optical excitation, equations (2) and (3) introduce non linearities that result in harmonics of the fundamental pulsation ω. Consequently, we can use the Fourier series decomposition, which is the decomposition of temporal functions on the orthogonal base $(e^{ik\omega t})_{-\infty < k < +\infty}$, k being an integer. Since we work with real functions, the coordinate on $e^{-ik\omega t}$ is the conjugate of the one on $e^{ik\omega t}$, and we can write:

$$\begin{cases} n = \sum_{k=-\infty}^{+\infty} \underline{n_k} e^{ik\omega t}, \\ n_t = \sum_{k=-\infty}^{+\infty} \underline{n_{t_k}} e^{ik\omega t}, \end{cases} \tag{10}$$

with :

$$\begin{cases} \underline{n_k} = n_k e^{i\phi_{n,k}}, \\ \underline{n_{t_k}} = n_{t_k} e^{i\phi_{t,k}}, \end{cases} \tag{11}$$

n_k and n_{t_k} being real quantities, and we have $\phi_{n,0} = 0$ and $\phi_{t,0} = 0$ so $\underline{n_0} = n_0$ and $\underline{n_{t_0}} = n_{t_0}$ which are the DC concentrations of free electrons and trapped electrons, respectively.

From our experience on a wide range of materials and experimental conditions, the amplitude of the harmonics ($k \geq 2$) in the PL signal is usually less than a few percent of the amplitude of the fundamental ($k = 1$). So, we make the hypothesis that the terms with $k \geq 2$ are negligible.

The photoluminescence signal is proportional to the radiative recombination rate, so :

$$PL = K.B.n.p, \tag{12}$$

K being a constant depending on the sample geometry and collecting area.

Using equation (1) to have only n and n_t as variables (and not p), together with equation (10), we can express the fundamental of PL as

$$\underline{PL_1} = K.B.\underline{n_1}.(N_a + 2.n_0 + n_{t_0}) + K.B.\underline{n_{t_1}}.n_0. \tag{13}$$

Then, we can inject equations (1) and (10) in equations (2) and (3), do their projection on $e^{i\omega t}$, and by orthogonality, and after rearrangement, we obtain :

$$\begin{pmatrix} A_1 & A_2 \\ A_3 & A_4 \end{pmatrix} \begin{pmatrix} \underline{n_1} \\ \underline{n_{t_1}} \end{pmatrix} = G_1 \begin{pmatrix} 1 \\ 1 \end{pmatrix}, \tag{14}$$

with

$$\begin{cases} A_1 = i\omega + v_{th}\sigma_n(N_t - n_{t_0}) + B(N_a + 2n_0 + n_{t_0}), \\ -A_2 = \omega_{r,e} + (v_{th}\sigma_n - B)n_0, \\ A_3 = i\omega + v_{th}\sigma_p n_{t_0} + B(N_a + 2n_0 + n_{t_0}), \\ A_4 = i\omega + v_{th}\sigma_p(N_a + n_0 + 2n_{t_0}) + Bn_0 + \omega_{r,h}. \end{cases} \tag{15}$$

By inverting the matrix, we obtain :

$$
\begin{cases}
\underline{n_1} = \dfrac{A_4 - A_2}{A_1 A_4 - A_2 A_3} . G_1, \\[4mm]
\underline{n_{t_1}} = \dfrac{A_1 - A_3}{A_1 A_4 - A_2 A_3} . G_1.
\end{cases}
\tag{16}
$$

According to the definition of the matrix elements A_{1-4}, it is necessary to know all DC quantities in order to evaluate the phase of n_1 and n_{t_1}, and thus the phase of the PL. These are obtained from the DC components of (2) and (3) :

$$
\begin{cases}
0 = G_0 - (N_a + n_0 + n_{t_0})v_{th}\sigma_p n_{t_0} - Bn_0 * (N_a + n_0 + n_{t_0}) \\
+(N_t - n_{t_0})\omega_{r,h} - 2v_{th}\sigma_p n_{t_1}^2 - 2Bn_1^2 - 2(v_{th}\sigma_p + B)n_{t_1}n_1 cos(\phi_{n,1} - \phi_{t,1}), \\
0 = G_0 + n_{t_0}\omega_{r,e} - n_0 v_{th}\sigma_n(N_t - n_{t_0}) - Bn_0 * (N_a + n_0 + n_{t_0}) - 2Bn_1^2 \\
+2(v_{th}\sigma_n - B)n_{t_1}n_1 cos(\phi_{n,1} - \phi_{t,1}).
\end{cases}
\tag{17}
$$

We see a coupling between order 0 and order 1, the DC terms are dependent on ω, which means that the system is not linear.

Due to non-linearities and coupling, it is not possible to obtain simple analytical solutions for these DC concentrations. However, the system of equations (16) and (17) can be solved numerically.

We define ω_0, S, ω_1, ω_2, ω_{2bis} and ω_3 by the following equations :

$$
\begin{cases}
\omega_0^2 = (A_1 - i\omega)(A_4 - i\omega) + (-A_2)(A_3 - i\omega), \\
S = (A_1 - i\omega) - A_2 + (A_4 - i\omega), \\
\omega_1\omega_3 = \omega_0^2, \\
\omega_1 + \omega_3 = S, \\
\omega_2 = (A_4 - i\omega) - A_2 = \omega_{r,e} + v_{th}\sigma_n n_0 + v_{th}\sigma_p(N_a + n_0 + 2n_{t_0}) + \omega_{r,h}, \\
\omega_{2bis} = A_1 - A_3 = v_{th}\sigma_n(N_t - (1 + \frac{\sigma_p}{\sigma_n})n_{t_0}).
\end{cases}
\tag{18}
$$

From that definition, ω_1 and ω_3 can be complex numbers, but we suppose that they are real and positive (which is true as far as we know, and we show it in Appendix A for a typical case).

Using (18), we can write (16) the following way

$$
\begin{cases}
\underline{n_1} = \dfrac{i\omega + \omega_2}{(i\omega)^2 + S.i\omega + \omega_0^2}G_1 = \dfrac{\omega_2 G_1}{\omega_1\omega_3}\dfrac{(1 + i\omega/\omega_2)}{(1 + i\omega/\omega_1)(1 + i\omega/\omega_3)}, \\[3mm]
\underline{n_{t_1}} = \dfrac{\omega_{2bis}G_1}{\omega_1\omega_3}\dfrac{1}{(1 + i\omega/\omega_1)(1 + i\omega/\omega_3)}.
\end{cases}
\tag{19}
$$

From that, the phase shift of $\underline{n_1}$ is

$$
\phi_{n,1} = -\arctan(\omega/\omega_1) + \arctan(\omega/\omega_2) - \arctan(\omega/\omega_3),
\tag{20}
$$

and, from (13), the phase shift of the PL is :

$$
\phi_{PL} = arg(\underline{PL_1}) = -\arctan(\omega/\omega_1) + \arctan(\omega/\omega_{2ter}) - \arctan(\omega/\omega_3),
\tag{21}
$$

with ω_{2ter} depending on ω_2 and ω_{2bis} :

$$
\omega_{2ter} = \omega_2 + \dfrac{n_0}{Na + 2.n_0 + n_{t_0}}\omega_{2bis}.
\tag{22}
$$

In equations (18) to (22) the quantities ω_1, ω_2, ω_{2ter} and ω_3 are dependent on ω due to the coupling between orders 0 and 1 in (17). If we can consider them constant, then the analytical model highlights three corner frequencies, so that it can appears "V-shapes", with a local extremum, due to ω_2. But it may appear more complex cases if they present significant variations. Now, we will see some approximations to see the meaning of the corner frequencies in low-illumination conditions.
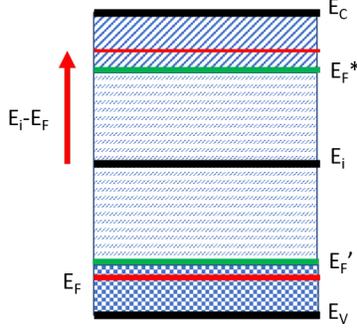
Figure 2: The three considered areas of energy position of the defect, delimited by E'_F and E^*_F defined in equation (25)

II.2 Low-illumination approximation

We define the low-illumination conditions by

$$n_0 \ll N_a, \tag{23}$$

and (at least) one of these two conditions

- $n_{t_0} \ll min(N_t, N_a)$,

- $n_{t_1} \ll n_{t_0}$.

We show in Appendix B that in such conditions $\omega_{2ter} \simeq \omega_2$ and that we can neglect coupling terms between orders 0 and 1 in (17). From that, we can deduce that n_0 and n_{t_0} are independent from ω, and that the same is true for ω_1, ω_2, ω_{2ter} and ω_3. Then, from (17), n_{t_0} is given by :

$$\frac{n_{t_0}}{N_t} = \frac{\omega_{r,h} + v_{th}\sigma_n n_0}{\omega_{r,h} + v_{th}\sigma_p p_0 + \omega_{r,e} + v_{th}\sigma_n n_0}. \tag{24}$$

In the following, we will divide the bandgap in three regions, as can be seen on figure 2, which are delimited by the two levels E'_F and E^*_F, defined by

$$\begin{cases} E'_F = E_F + k_B T \ln(1 + N_t/N_a), \\ E^*_F = E_i + (E_i - E_F) - k_B T \ln(\sigma_n/\sigma_p), \end{cases} \tag{25}$$

which can be considered as demarcation levels.

If $E_t > E^*_F$, the defect can be considered as a minority carrier trap (here an electron trap). If $E'_F < E_t < E^*_F$, it can be regarded as a recombination center. Finally, if $E_t < E'_F$, it can be considered as a majority carrier trap (here a hole trap). In the following, we will consider these three cases where further approximation can be done, which leads in particular to the demonstration of a V-shape in the phase plot in the first case only.

Minority carrier (electron) trap

We have :

- $E_t > E'_F$, so that we consider that the condition $n_{t_0} \ll min(N_t, N_a)$ is fulfilled,

- $E_t > E^*_F$, so that $n_t \omega_{r,e} \gg p\omega_{c,h}$.

So, when the energy level is in this region, less holes are captured than electrons are released by the defect, so the defect is doing trapping and detrapping. .

Then, we have :

$$
\begin{cases}
\omega_2 = \omega_{r,e}, \\
S = \omega_{c,e} + \omega_{rad} + \omega_2, \\
\omega_0^2 = \omega_{c,e} v_{th} \sigma_p N_a + \omega_{rad} \omega_2.
\end{cases}
\tag{26}
$$

We need to distinguish two cases. If radiative recombination is dominant (a sufficient condition is $\omega_{c,e} \ll \omega_{rad}$), then

$$
\begin{cases}
S = \omega_{rad} + \omega_2, \\
\omega_0^2 = \omega_{rad} \omega_2.
\end{cases}
\tag{27}
$$

So the expression of the phase shift is really simple :

$$
\phi_{n,1} = -\arctan(\omega/\omega_{rad}).
\tag{28}
$$

Now, if we have $\omega_{rad} \ll S$, let's consider :

$$
\omega_* = (v_{th} \sigma_p N_a + \omega_{rad} \frac{\omega_{r,e}}{\omega_{c,e} + \omega_{rad}}) \frac{\omega_{c,e} + \omega_{rad}}{\omega_2 + \omega_{c,e} + \omega_{rad}}.
\tag{29}
$$

Then, it appears that

$$
\begin{cases}
\omega_0^2 = S \omega_*, \\
\omega_* \ll S.
\end{cases}
\tag{30}
$$

So that

$$
\begin{cases}
\omega_1 = \omega_*, \\
\omega_2 = \omega_{r,e}, \\
\omega_3 = S.
\end{cases}
\tag{31}
$$

It means that there are three distinct corner pulsations and that the phase diagram presents a V-shape.

Recombination center

We have :

- $E_t > E'_F$, so that we consider that the condition $n_{t_0} \ll min(N_t, N_a)$ is fulfilled,

- $E_t < E_F^*$, so that $n_t \omega_{r,e} \ll p \omega_{c,h}$.

We can derive :

$$
\begin{cases}
\omega_1 = \omega_2 = v_{th} \sigma_p N_a, \\
\omega_3 = \omega_{c,e} + \omega_{rad}.
\end{cases}
\tag{32}
$$

So, the expression of the phase shift is :

$$
\phi_{n,1} = -\arctan(\omega/(\omega_{c,e} + \omega_{rad})).
\tag{33}
$$

The corner pulsation we measure $(\omega_{c,e} + \omega_{rad})$ is the inverse of what we usually named the lifetime of the sample. So, from the phase plot, we can directly know the lifetime.

One can see that the energy level and the hole capture cross-section have no influence on the phase plot, contrary to the electron capture cross-section and the density of traps.

Layer Thickness (μm)	2,3
Bandgap E_g (eV)	1,2
P-type doping N_a (cm^{-3})	3.10^{16}
Conduction and valence band density of states N_c/N_v (cm^{-3})	2.10^{18}
Electron affinity (eV)	4,1
Relative permittivity ϵ_r	13,6
Electron mobility μ_n (cm^2.V^{-1}.s^{-1})	50
Hole mobility μ_p (cm^2.V^{-1}.s^{-1})	20
Radiative recombination coefficient B (cm^3/s)	8.10^{-11}
k_BT (eV)	0,0258
v_{th} (cm/s)	1.10^7

Table 1: Parameters used for the model

Majority carrier (hole) trap

In that case we cannot neglect n_{t_0} anymore in front of N_a or N_t in the dark. So, we use the condition $n_{t_1} \ll n_{t_0}$.

Then, we can make the following approximation :

$$\begin{cases} \omega_1 = \omega_2 = \omega_{r,h} + v_{th}\sigma_p(N_a + 2n_{t_0}), \\ \omega_3 = \omega_{c,e} + \omega_{rad} = v_{th}\sigma_n(N_t - n_{t_0}) + B(N_a + n_{t_0}), \end{cases} \tag{34}$$

so that the expression of the phase is :

$$\phi_{n,1} = -\arctan(\omega/(\omega_{c,e} + \omega_{rad})). \tag{35}$$

We obtain the same equation as for a recombination center, but here we cannot neglect the impact of n_{t_0} in the expression of the corner frequency.

From this development, in low-illumination conditions, the phase plot can be described by an arc-tangent in the cases of a recombination center and of a majority carrier trap. It implies that we cannot differentiate between them, and that the same phase plot can be obtained for different set of parameters. It is a limit of this characterization technique, at least as long as we stay in low-injection conditions. Another limit is that when there is only one corner frequency, we cannot know so much about the defect parameters (density, energy position, capture cross-sections).

We have also shown that in low illumination conditions the corner frequencies are independent from the illumination power.

III   Assessment from numerical modeling

Here we first test the validity of the analytical approach developed in section II with the help of a full numerical modeling. We use the Atlas software, from Silvaco Inc., which computes currents and concentrations of carriers numerically in each point of a user-defined mesh by solving Poisson's and continuity equations using a finite difference method. The parameters we use for the modeling of the material are specified in Table 1. These parameters are taken here as an example that is representative of a CIGS thin film. The layer is not connected to an external circuit, so it is in open-circuit conditions. We define a modulated photogeneration with a modulation depth of 100%, and the absorption is considered to follow Beer-Lambert's law:

$$G(y) = G_0(1 + \sin(2\pi ft)). \exp(-\alpha y), \tag{36}$$

where y is the coordinate perpendicular to the illuminated surface ($y = 0$, figure 1a), α the absorption coefficient, G_0 the generation rate at the surface, and f the frequency. We introduce one defect level in the bandgap, the energy of which will be varied, along with the capture cross sections. Exchanges between this level and the conduction and valence bands are considered through detailed balance, and an additional radiative recombination is also considered, however we have neglected Auger recombination. For radiative recombination, the model is very simple, without taking into account the spectrum of luminescence nor any optical aspect. All the details are given in the user's manual [17]. We also add surface recombination recombination modeled by a surface recombination velocity (SRV). Except where it is precised, SRV will refer to the surface recombination velocity of electrons (the minority carriers) the value of which being described by s_n.

The photoluminescence is computed by the software as the integral of the radiative recombination rates over the whole thickness of the sample. In a first part of the simulation, all equations are time-resolved, and then, when the steady-state is reached, a fast Fourier transform (FFT) is performed (on the steady-state part) to extract the phase shift of the fundamental of the PL compared to the photogeneration. We then plot the phase as a function of frequency and we fit it with a sum of up to three arc-tangents as defined in equation (21), with a dedicated spreadsheet software, and then, if needed, the characteristic frequencies - also called corner frequencies in the following, are optimized with an elementary algorithm to yield the best fit.

In a first part, we will consider uniform generation ($\alpha = 0$), with negligible surface recombination (s_n=1cm/s) to have a direct comparison with the analytical model described in Section II, then we will consider $\alpha = 1, 4.10^5 \text{cm}^{-1}$, which is the value measured at 532 nm in [13], in order to show that the analytical model can still be used in non-uniform illumination. Finally, we will increase surface recombination and study its impact on the phase of the photoluminescence.

The numeration of the curves refers to Table 2 where one can find the parameters of the simulations (energy position of the defect, its electron and hole capture cross-sections, its density, and the surface recombination velocity), and the computed corner frequencies are gathered in Table 3. These corner frequencies can be compared with the analytical values given in Table 4, where one can also find the value of $E_F^*, \omega_{c,e}, \omega_{r,e}, \omega_{r,h}$, and ω_{sn}.

III.1 Homogeneous photogeneration without SRV

In order to assess the validity of the analytical calculations of Section II, here we take $\alpha = 0$, with negligible surface recombination (s_n=1cm/s), and a nominal generation rate G_0= 2,2.10^{19} cm^{-3}.s^{-1}.

On figure 3 we show the phase plots when the defect acts as a recombination center. Simulations C1, C2 and C3 correspond to the same energy level ($E_t = E_c - 0, 3$ eV) and different electron capture cross-sections, 1.10^{-18}, 1.10^{-16} and 1.10^{-14} cm^2, respectively, while in C4 the defect level position is deeper in the band gap, with $E_t = E_c - 0, 6$eV and $\sigma_n = 1.10^{-14}$ cm^2. Simulations have been verified to be in the low-injection regime. For instance, for C5, we obtain $n_0 = 1, 8.10^{12}$ cm^{-3} and $n_{t0} = 5, 7.10^{13}$ cm^{-3}. So, we are in the case of equation (23) with $n_{t_0} \ll min(N_t, N_a)$. Note that, unless otherwise stated, all the next results are obtained in low-injection conditions. As expected from our analytical model, one can observe only one corner frequency in the phase plots. The values of the corner frequencies are consistent with our computations (equation (32)). For C1, we can only distinct the radiative lifetime ($4, 2.10^{-7}$s) because it is much smaller than the capture one (1.10^{-5}s). On the contrary, for C3 only the capture time (1.10^{-9}s) of the defect is visible. We see that we obtain the same plot for C3 and C4. This is due to the fact that for a recombination center, the value of the corner frequency depends only on σ_n and N_t, which are the same for both cases.

As discussed in Section II, not all defects act as recombination centers. When we place a defect near the conduction band with a large electron capture cross-section compared to the hole one, we have an electron trap ($E_t > E_F^*$). As predicted by our analytical modeling, the phase plots exhibit V-shapes, as we can see on figure 4, with three corner frequencies, except for C7 which corresponds to a lower N_t (1.10^{14}cm^{-3}). One can also check that the equations derived in the analytical modeling section (especially (31)) yield correct quantitative results. For C7, the radiative component is dominant, so only the radiative lifetime is visible, as explained in equation (27). On these examples, we can easily identify the corner frequencies for C5 and C6, corresponding to a defect density of 1.10^{16}cm^{-3}, and 1.10^{15}cm^{-3}, respectively. However, for C7, where the defect density was decreased to 1.10^{14} cm^{-3}, the defect is invisible, radiative recombination prevails and the phase diagram is the same as without defect, with a
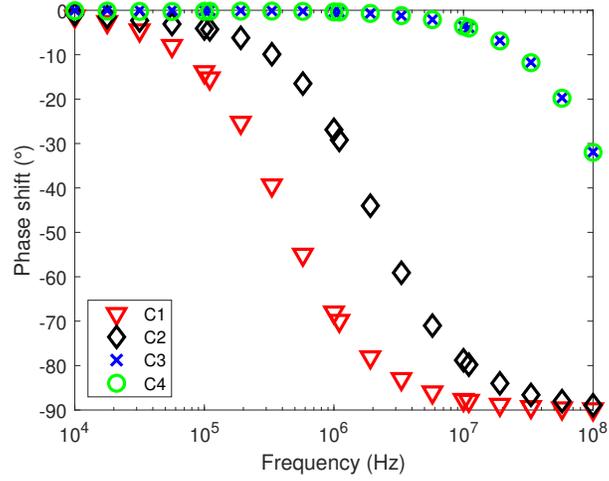
Figure 3: Phase diagrams of simulation cases C1, C2, C3, C4, where the defect level acts as a recombination center. Simulations have been performed under homogeneous generation and without SRV.
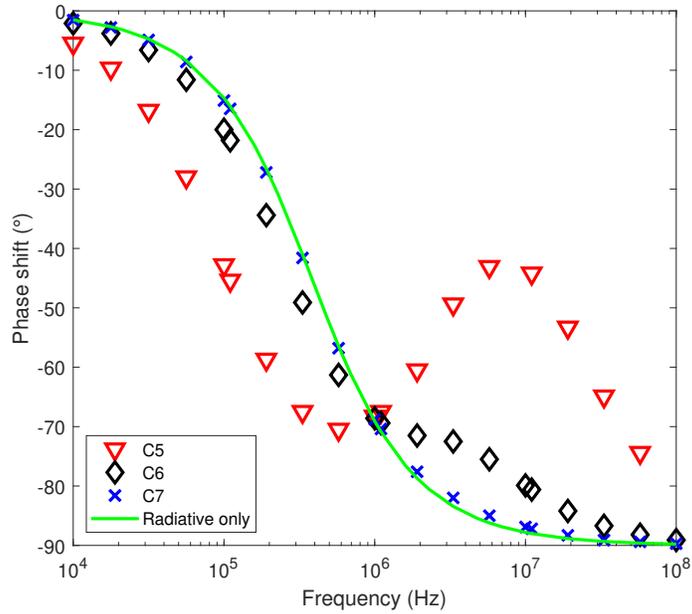

Figure 4: Phase diagrams of simulation cases C5, C6, C7, where the defect level acts as a minority carrier trap. Simulations have been performed under homogeneous generation and without SRV. The full line represents the result of the simulation without defect level, with only radiative recombination.
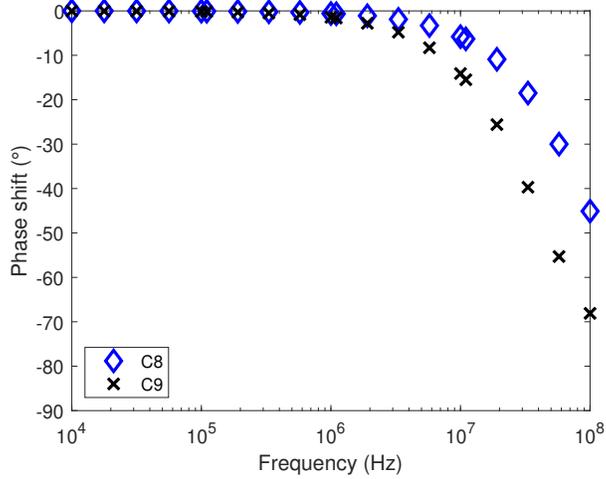
Figure 5: Phase diagrams of simulation cases C8 and C9, where the defect level acts as a majority carrier trap. The simulations have been performed under homogeneous generation and without SRV.

single arc tangent function and a single corner frequency corresponding to the radiative lifetime. This emphasizes that significant trapping/detrapping is required to be distinguished as a V-shape in the phase diagram.

In figure 5 we show the phase diagram when the defect level has been set close to the valence band, corresponding to C8 and C9. In agreement with the analytical analysis, the phase diagram exhibits a single arc tangent behaviour. For C8, the obtained corner frequency of 1.10^8Hz is in good agreement with that calculated from equation (35) (9.10^7Hz), taking into account the value of n_{t_0}, calculated in the dark from equation (24) with $n_0 = 0$. For C9, the obtained corner frequency is 4.10^7Hz, close to the analytical model result of $4,3.10^7$Hz. Without taking into account n_{t_0}, we would have found a significantly larger value, $1,6.10^8$Hz, which illustrates the correction in the corner frequency in the case of a majority carrier trap compared to a defect acting as a recombination center.

The cases C10, C11 and C12 correspond to the same electron trap configuration as C5, but we increased the generation rate to G_0= $2,2.10^{20}$, $2,2.10^{21}$, and $2,2.10^{22}$cm^{-3}s^{-1}, respectively. The comparison is shown in figure 6. We observe that in low-injection the phase diagram is independent of the injection level (the curves are identical for C10 and C5). But, when the injection is high enough, the hypothesis of low-illumination $n_{t_0} \ll \min(N_t, N_a)$ is no longer respected. Indeed, we obtain for C11 $n_0 = 5,5.10^{14}$cm^{-3} and $n_{t_0} = 2,2.10^{15}$cm^{-3}. n_{t_0} is no longer negligible compared to N_t, so it impacts the capture time ($\omega_{c,e}$) and we have $v_{th}\sigma_n n_0 = 5,5.10^6$ rad/s which is not negligible compared to ω_2. We have approximately :

$$\begin{cases} \omega_2 \simeq \omega_{r,e} + v_{th}\sigma_n n_0 = 2,5.10^7 \text{ rad/s } (3,9.10^6\text{Hz}), \\ \omega_3 \simeq \omega_2 + v_{th}\sigma_n(N_t - n_{t_0}) = 1.10^8 \text{ rad/s } (1,6.10^7\text{Hz}). \end{cases} \quad (37)$$

The corner frequencies extracted from the simulations are in very good agreement with these analytical approximate expressions. Indeed, we find f_2=$3,9.10^6$ Hz instead of 4.10^6 Hz and f_3= $1,6.10^7$ Hz instead of $1,7.10^7$ Hz.

For C12, we see that the V-shape is less visible, because ω_2 increases due to n_0, and $\omega_{c,e} = v_{th}\sigma_n(N_t - n_{t_0})$ becomes smaller. We have $n_0 = 5,4.10^{15}$cm^{-3} and $n_{t_0} = 7,3.10^{15}$cm^{-3}. The following analytical equations approximate very well the simulated corner frequencies (f_1=$4,8.10^5$ Hz, f_2=$1,1.10^7$ Hz and f_3=$1,5.10^7$ Hz) :

$$\begin{cases} \omega_1 \simeq B(N_a + n_{t_0}) = 3.10^6 \text{ rad/s } (4,8.10^5\text{Hz}), \\ \omega_2 \simeq \omega_{r,e} + v_{th}\sigma_n n_0 = 7,3.10^7 \text{ rad/s } (1,2.10^7\text{Hz}), \\ \omega_3 \simeq \omega_2 + v_{th}\sigma_n(N_t - n_{t_0}) = 1.10^8 \text{ rad/s } (1,6.10^7\text{Hz}). \end{cases} \quad (38)$$
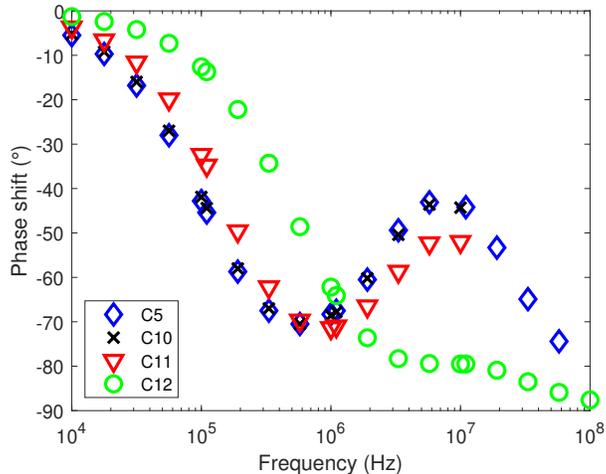
11

Figure 6: Phase diagrams of simulation cases C5, C10, C11, C12 where the defect level acts as a minority carrier trap, for increasing generation rates. Simulations have been performed under homogeneous generation and without SRV.

III.2 Non homogeneous photogeneration without SRV

When we simulate a more realistic non homogeneous photogeneration with $\alpha = 1,4.10^5 \mathrm{cm}^{-1}$, we obtain the same results as those obtained with an homogeneous photogeneration. We can explain this by the fact that, although the generation profile is not homogeneous, the concentration of charge carriers is homogeneous, as we can see on figure 7b for a frequency of $1.10^5 \mathrm{Hz}$ for the case C5, with the moments expressed in terms of generation level, for the rising (up) and falling (down) parts of the sinusoid. This is because the carriers can homogenize across the layer thickness. Indeed with the mobility values and thickness chosen here, we expect the carriers to be able to homogenize for frequencies below 10 MHz. Even between 10 MHz and 100 MHz, we observed that the phase of the PL was modified by less than a few degrees compared to the homogeneous generation. This is due to the fact that we consider low-illumination conditions, so that the lifetimes are nearly independent from the concentration of carriers. The ability for the carriers to homogenize has been also assessed by further increasing the absorption coefficient, so that the photogeneration is only on the surface, where no significant change was observed in the carrier concentration profile and in the phase of the PL. Consequently, we can say that our hypothesis of neglecting the Beer-Lambert's law in our analytical approach is valid, and there is no significant impact of either the absorption coefficient or the thickness of the sample, as long as low-illumination conditions are fulfilled in each point of the sample and that we can neglect re-absorption.

III.3 With SRV

We now increase the surface recombination. Depending on the ability of transport to homogenize the carrier distributions, this may produce space-dependent carrier concentrations, so that the main hypothesis of homogeneity is challenged. A classical way to transpose SRV into a bulk equivalent while keeping the hypothesis of homogeneity, is to consider another recombination term to take account of this additional recombination path in the continuity equations (2) and (3), which can be expressed as $-n.\omega_{sn}$, with ω_{sn} defined by [3][4] :

$$\omega_{sn} = \frac{2.s_n}{d}, \tag{39}$$

with d the thickness of the sample.

First, we consider only radiative recombination and surface recombination without any bulk defect. In C13 and C14, the surface recombination velocity s_n was taken equal to values of 1.10^3 and 1.10^5 cm/s, respectively. The phase diagrams are compared in figure 8. We observe that the corner frequency increases with s_n. This was expected because it means that the effective lifetime decreases. When s_n is low (1.10^3cm/s), we see only one corner

(a) (b)

Figure 7: Photogeneration and density of electrons as a function of time (a) and density of electrons at different moments during one period at 1.10^5Hz as a function of the depth in the sample (b). The black lines on (a) shows the different moments of (b).

Figure 8: Phase diagrams of simulation cases C13 and C14, without any bulk defect and two values of surface recombination velocities (1.10^3 and 1.10^5 cm/s, respectively). The plain line shows the result for negligible surface recombination, with the only radiative recombination.

Figure 9: Phase diagrams of simulation cases C15 and C16, with a bulk defect level acting as a recombination center ($E_t = E_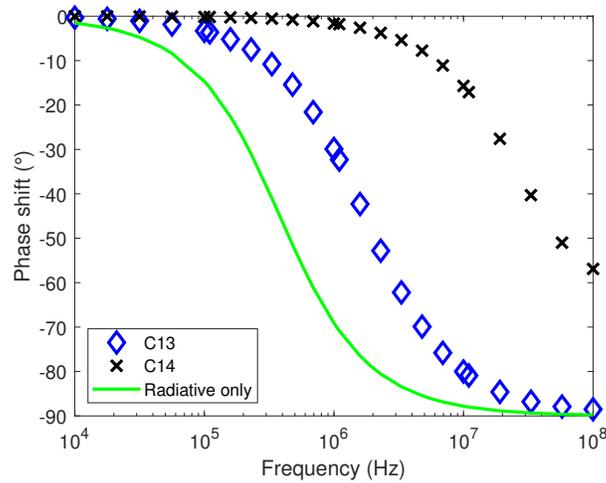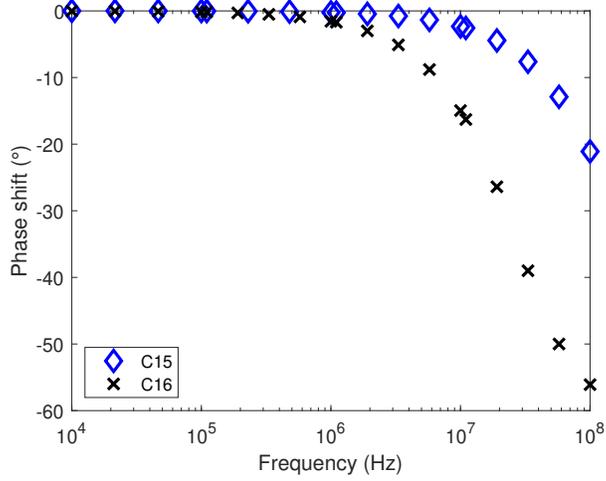c - 0,6$ eV) for electron capture cross sections of 1.10^{-14} and 1.10^{-16} cm^2, respectively. The surface recombination velocity was set to $s_n = 1.10^5$cm/s.

frequency that can be identify with :

$$\omega_1 = 2\pi f_1 = \omega_{rad} + \omega_{sn}. \tag{40}$$

For high values of s_n, 1.10^5cm/s or higher, the fit with a single arc tangent function is not good and requires the sum of three arc tangent functions. Indeed, the diffusion phenomenon is visible at high frequency and limits the recombination rate at the surface and so the corner frequency. From [18] and [19] we have the following equations :

$$\begin{cases} \omega_1^{-1} = \omega_{diff}^{-1} + \omega_{sn}^{-1}, \\ \omega_3 = \omega_{sn}, \end{cases} \tag{41}$$

with

$$\omega_{diff} = \frac{\pi^2}{d^2/D}, \tag{42}$$

and D is the diffusion coefficient related to the mobility through Einstein's relation

$$D = \mu \frac{k_B T}{q}. \tag{43}$$

The determination of ω_3 is not very precise here since its impact is rather at frequencies beyond the scanned ones (i.e. larger than 1.10^8Hz), while for ω_2, no equation has been found.

Some techniques exist to determine surface recombination velocities using TRPL with different excitation wavelengths (so that the absorption coefficient changes) [20]. A similar protocol might be explored with HF-MPL, combined with changing the excitation intensity, to separate the contributions of surface and bulk recombinations.

We now add a bulk defect level acting as a recombination center. Simulations C15 and C16 correspond to a defect level at $E_t = E_c - 0,6$ eV with an electron capture cross-section equal to 1.10^{-14} and 1.10^{-16} cm^2, respectively, while a surface recombination velocity of $s_n = 1.10^5$cm/s was taken into account. Like in the radiative case, in figure 9 we observe that the corner frequency is increased compared to the figure 3 and that the diffusion makes the curves more complex. In that case, we fit them with 5 arctangent functions. To compute analytically the corner frequencies, we add a recombination term in equations (2) and (3) which takes into account SRV and diffusion. It leads to slight modifications of the expressions of the three corner frequencies expressed in (18), and we introduce $\omega_5 = \omega_{sn}$ when it is needed. No equation has been found for ω_4.

Finally, we consider the effect of SRV in the case of a bulk electron trap ($E_t = E_c - 0,18$ eV). Simulations C17, C18 and C19 are obtained for surface recombination velocities $s_n = 1.10^3$, 1.10^5, and 1.10^7 cm/s, respectively, and
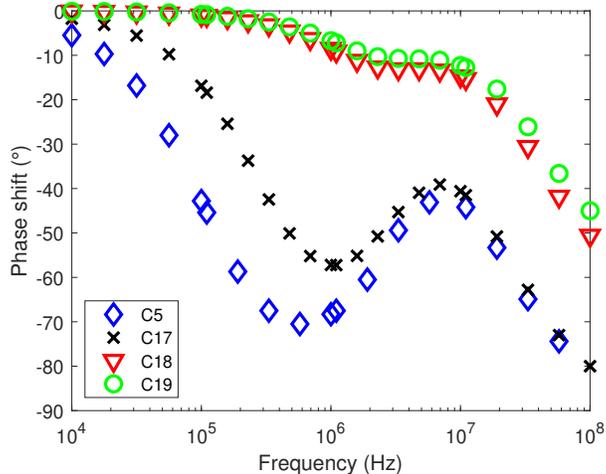
Figure 10: Phase diagrams of simulation cases C5, C17, C18, C19, with a bulk defect level acting as a minority carrier trap, for increasing values of surface recombination velocity, $s_n = 1, 1.10^3, 1.10^5,$ and 1.10^7 cm/s, respectively.

they are compared on figure 10 to the case C5 studied before of negligible surface recombination, $s_n = 1$ cm/s. We note that the second corner frequency, linked to the release time, is independent of the SRV. This is compatible with the modification of (2) and (3) with ω_{sn} as suggested before (not linked to n_t). Like in the radiative case, we can distinguish between low SRV and high SRV. As written in Table 3, C19 has been fitted with only four arctangent functions instead of five, because the fifth one has little impact on the diagram.

So far, we have considered that the SRV is the same on both surfaces, but its impact on the front face, where the photogeneration is the highest, is not the same as on the back face. Simulations C20 and C21 are obtained for the same electron trap level as C5 and C18, but with asymmetric surface recombination velocities : SRV_{front} = 1cm/s and SRV_{back}=1.10⁵cm/s for C20, and SRV_{front} = 1.10^5cm/s and SRV_{back}=1cm/s for C21. These two values corresponding to the symmetric values taken in C5 and C18. In figure 11, we can see that the phase diagrams corresponding to C20 and C21 are the same as that of C18 (high symmetric values of SRV) at low frequency, while at high frequency C20 is similar to the case of C5 (low symmetric value of SRV) whereas C21 is similar to C18. This illustrates that the hypothesis of homogeneity depends on the frequency of excitation, and that at high frequency we are more sensitive to what happens in the front part, considering that generation rate is higher at the front surface.

IV   Comparison with experimental data

To illustrate the above developments, we will perform an analysis of an experimental result from a sample of CIGS at low-injection.

The experimental setup we have used is based on a conventional PL microscopy scheme. A sketch of it can be seen on figure 12. The light source is a fast modulated laser at 638 nm. The modulation is based on sinusoidal variations of the light intensity around a given working point. In this study the ratio between modulated and continuous part of the modulated light is close to 60%, however the response of the sample remains sufficiently linear, the second harmonic being less than 3% of the fundamental signal. The light is sent to the system via an injection fiber with 100 μm core. A lens is placed at the output of the fiber and allows for collimating the laser beam in a horizontal direction. Then a dichroic mirror sends the light to the sample vertically. The following lens allows for focusing on the sample which is at the bottom of the system. The beam size on the sample was measured to be 200 μm. The photoluminescence signal is then collected via the dichroic mirror and supplementary long pass filters vertically and sent into a 100 μm core multimode fiber. The lens focusing into the last fiber is chosen so that we probe a 50 μm area inside the illuminated area, avoiding diffusion effects. To detect the signal with an optimal sensitivity we used a single photon avalanche detector. Then a Picoharp 300 time Correlated Single Photon Counter (TCSPC) and a LabVIEW software allow for reconstructing one period of the modulated signal. Once
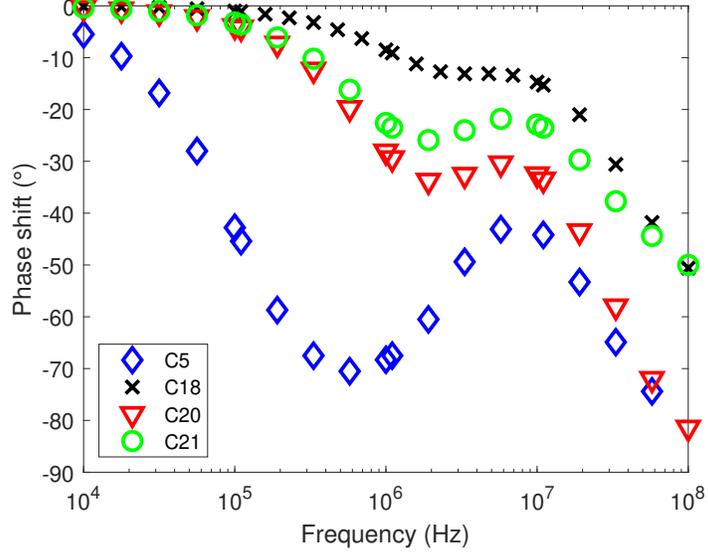
Figure 11: Phase diagrams of simulation cases C20 and C21, with high (resp. low) SRV on back surface and low (high) SRV on front surface, compared to the C5 and C18 with symmetric low and high surface recombination velocities, respectively. In all cases the same bulk electron trap properties were considered.

curve	Ec-Et (eV)	-log(σ_n/1cm^2)	-log(σ_p/1cm^2)	log(N_t/1cm^{-3})	SRV s$_n$ (cm/s)
C1	0,3	18	18	16	1
C2	0,3	16	18	16	1
C3	0,3	14	14	16	1
C4	0,6	14	18	16	1
C5	0,18	15	18	16	1
C6	0,18	15	18	15	1
C7	0,18	15	18	14	1
C8	1,1	15	18	17	1
C9	1,15	15	18	17	1
C10 (G×10)	0,18	15	18	16	1
C11 (G×100)	0,18	15	18	16	1
C12 (G×1000)	0,18	15	18	16	1
C13	x	x	x	x	1.10^3
C14	x	x	x	x	1.10^5
C15	0,6	14	14	16	1.10^5
C16	0,6	16	14	16	1.10^5
C17	0,18	15	18	16	1.10^3
C18	0,18	15	18	16	1.10^5
C19	0,18	15	18	16	1.10^7
C20	0,18	15	18	16	$1/1.10^5$
C21	0,18	15	18	16	$1.10^5/1$

Table 2: Summary table of simulation parameters

16

curve	type of simulation	f_1 (Hz)	f_2 (Hz)	f_3 (Hz)	f_4 (Hz)	f_5 (Hz)
C1	recombination center (defect invisible)	4.10^5				
C2	recombination center	2.10^6				
C3	recombination center	$1,6.10^8$				
C4	recombination center	$1,6.10^8$				
C5	trap	1.10^5	3.10^6	$1,9.10^7$		
C6	trap	$2,6.10^5$	3.10^6	$4,8.10^6$		
C7	trap (defect invisible)	$3,8.10^5$				
C8	hole trap	9.10^7				
C9	hole trap	4.10^7				
C10	trap	1.10^5	3.10^6	$1,9.10^7$		
C11	trap	$1,5.10^5$	4.10^6	$1,7.10^7$		
C12	trap	$4,8.10^5$	$1,1.10^7$	$1,5.10^7$		
C13	radiative+SRV	$1,8.10^6$				
C14	radiative+SRV	3.10^7	$8,5.10^7$	$1,38.10^8$		
C15	rec. center+SRV	$2,5.10^8$				
C16	rec. center+SRV	$3,2.10^7$	$8,5.10^7$	$1,4.10^8$		
C17	trap+SRV	3.10^5	3.10^6	2.10^7		
C18	trap+SRV	2.10^6	3.10^6	$4,9.10^7$	9.10^7	$1,4.10^8$
C19	trap+SRV	$2,2.10^6$	3.10^6	$5,8.10^7$	$3,5.10^8$	
C20	trap+SRV	1.10^6	3.10^6	$2,3.10^7$		
C21	trap+SRV	$1,1.10^6$	$2,6.10^6$	$2,9.10^7$	$7,5.10^7$	$1,85.10^8$

Table 3: Corner frequencies obtained from a fit to the phase diagrams calculated from full numerical modeling

the modulated signal is recorded, we can extract the phase and amplitude of the first harmonic. Note that the phase of the laser modulation is also recorded prior to any measurement by replacing the sample by a mirror and the long-pass filter by a neutral density one. The phase presented here is thus the phase shift between PL and light excitation. Using a TCSPC allow for a high sensitivity from a few hundred hertz to 200 MHz which is the modulation limit of the laser.

The comparison of the experimental result and the fit according to our analytical model with the sum of three arc tangent functions is shown in figure 13.

We find the following values for the three corner frequencies:

$$\begin{cases} f_1 = 1,4.10^4 \text{ Hz}, \\ f_2 = 6,5.10^4 \text{ Hz}, \\ f_3 = 2,2.10^8 \text{ Hz}. \end{cases} \quad (44)$$

As we see a V-shape, we can deduce that this case corresponds to the case of a minority carrier trap (electron trap) as described in the modeling sections. Neglecting surface recombinations, we can use the following equations :

$$\begin{cases} \omega_1 = (v_{th}\sigma_p N_a + \omega_{rad}\dfrac{\omega_{r,e}}{\omega_{c,e} + \omega_{rad}}) * \dfrac{\omega_{c,e} + \omega_{rad}}{\omega_2 + \omega_{c,e} + \omega_{rad}}, \\ \omega_2 = \omega_{r,e} + v_{th}\sigma_p N_a, \\ \omega_3 = \omega_{c,e} + \omega_{rad} + \omega_2. \end{cases} \quad (45)$$

We take the values of radiative recombination coefficient (B) and doping acceptor concentration (N_a) in Table 1, so that $\omega_{rad} = 2,4.10^6$ rad/s. Then we can simplify equations (45), and we find :

17

curve	$E_c - E_F*$ (eV)	$\omega_{c,e}$	$\omega_{r,e}$	$\omega_{r,h}$	ω_{sn}	f_1 (Hz)	f_2 (Hz)	f_3 (Hz)	f_5 (Hz)
C1	0,11	1.10^5	$1,8.10^2$	$1,4.10^{-8}$	$8,7.10^3$	$4,8.10^4$	$4,8.10^4$	4.10^5	
C2	0,23	1.10^7	$1,8.10^4$	$1,4.10^{-8}$	$8,7.10^3$	$4,8.10^4$	$5,1.10^4$	2.10^6	
C3	0,11	1.10^9	$1,8.10^6$	$1,4.10^{-4}$	$8,7.10^3$	$1,6.10^8$	$4,8.10^8$	$4,8.10^8$	
C4	0,11	1.10^9	16	$1,6.10^{-3}$	$8,7.10^3$	$4,8.10^4$	$4,8.10^4$	$1,6.10^8$	
C5	0,29	1.10^8	$1,9.10^7$	$1,4.10^{-10}$	$8,7.10^3$	1.10^5	3.10^6	$1,9.10^7$	
C6	0,29	1.10^7	$1,9.10^7$	$1,4.10^{-10}$	$8,7.10^3$	$2,6.10^5$	3.10^6	$4,8.10^6$	
C7	0,29	1.10^6	$1,9.10^7$	$1,4.10^{-10}$	$8,7.10^3$	$3,6.10^5$	3.10^6	$3,2.10^6$	
C8	0,29	$6,2.10^8$	$6,1.10^{-9}$	$4,2.10^5$	$8,7.10^3$	$2,4.10^5$	$2,4.10^5$	1.10^8	
C9	0,29	$2,6.10^8$	$8,8.10^{-10}$	$2,9.10^6$	$8,7.10^3$	$7,4.10^5$	$7,4.10^5$	$4,3.10^7$	
C10	0,29	1.10^8	$1,9.10^7$	$1,4.10^{-10}$	$8,7.10^3$	1.10^5	$3,1.10^6$	$1,9.10^7$	
C11	0,29	$<1.10^8$	$1,9.10^7$	$1,4.10^{-10}$	$8,7.10^3$	$1,5.10^5$	$3,9.10^6$	$1,7.10^7$	
C12	0,29	$<1.10^8$	$1,9.10^7$	$1,4.10^{-10}$	$8,7.10^3$	$4,9.10^5$	$1,2.10^7$	$1,7.10^7$	
C13	x	x	x	x	$8,7.10^6$	$1,8.10^6$	x	x	
C14	x	x	x	x	$8,7.10^8$	3.10^7	?	$1,4.10^8$	
C15	0,11	1.10^9	16	16	$8,7.10^8$	$1,9.10^8$	$4,8.10^8$	$4,8.10^8$	
C16	0	1.10^7	$0,16$	16	$8,7.10^8$	$3,2.10^7$	$4,8.10^8$	$4,8.10^8$	$1,4.10^8$
C17	0,29	1.10^8	$1,9.10^7$	$1,4.10^{-10}$	$8,7.10^6$	$2,9.10^5$	3.10^6	2.10^7	
C18	0,29	1.10^8	$1,9.10^7$	$1,4.10^{-10}$	$8,7.10^8$	2.10^6	3.10^6	$4,7.10^7$	$1,4.10^8$
C19	0,29	1.10^8	$1,9.10^7$	$1,4.10^{-10}$	$8,7.10^{10}$	$2,1.10^6$	3.10^6	$5,5.10^7$	$1,4.10^{10}$
C20	0,29	1.10^8	$1,9.10^7$	$1,4.10^{-10}$	?	?	3.10^6	?	
C21	0,29	1.10^8	$1,9.10^7$	$1,4.10^{-10}$	?	?	3.10^6	?	?

Table 4: Analytical computation of the corner frequencies of the PL phase shift: $f_1 = \omega_1/2\pi$, $f_2 = \omega_{2ter}/2\pi$, $f_3 = \omega_3/2\pi$, using equations (18)-(22) for C1-C12, and equations (40) and (41) for C13-C14. For C15-C19, the equation (18) has been modified to take into account SRV and diffusion. The '?' indicate the absence of equations to calculate these values.
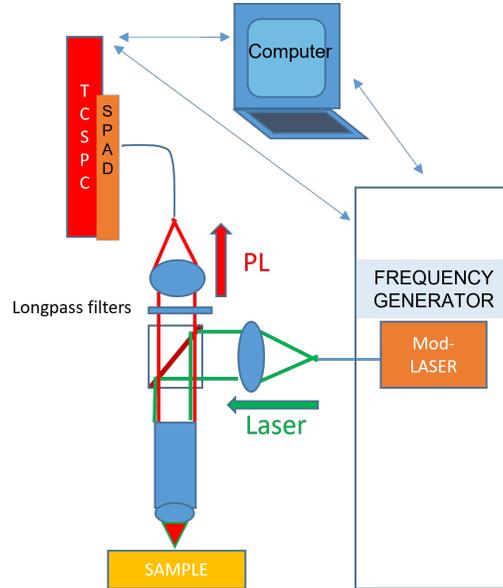

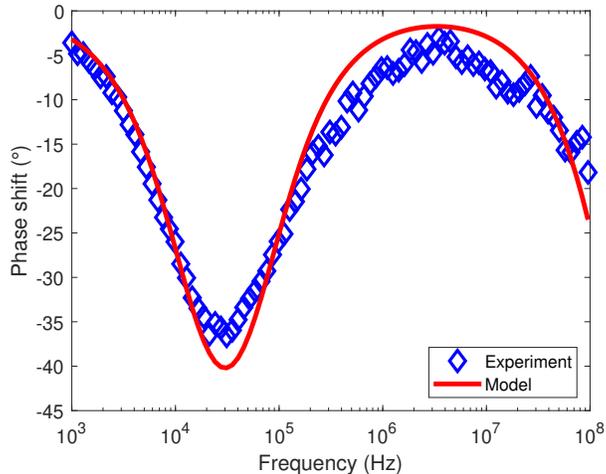Figure 12: Sketch of the experimental setup

Figure 13: Example of experimental phase diagram obtained on a CIGS sample and corresponding fit using our analytical model.

$$\begin{cases} \sigma_p = \dfrac{\omega_1}{v.N_a} = 3.10^{-19} \text{ cm}^2, \\[3mm] N_t\sigma_n = \dfrac{\omega_3}{v} = 140 \text{ cm}^{-1}, \\[3mm] \sigma_n n_i . \exp(\dfrac{E_t - E_i}{k_B T}) = \dfrac{\omega_2 - \omega_1}{v} = 0,032 \text{ cm}^{-1}. \end{cases} \tag{46}$$

We have three equations for four unknowns, so there is not a unique solution. Eventually, we managed to fit the diagram with the following parameters : $E_t = E_c - 0,26$ eV, $N_t = 3,7.10^{17}$cm^{-3}, $\sigma_n = 3,8.10^{-16}$cm^2, $\sigma_p = 3.10^{-19}$cm^2. These values are consistent with previous published results.[21] In order to increase the reliability of the extracted parameter values, one potential route is to perform experiments at excitation intensities beyond the low level injection and to use the simulation to study the dependence of the phase diagram on the excitation power. This of course is beyond the scope of this work and it deserves further studies.

V   Conclusion

In this work we have developed a simplified analytical approach of the MPL experiment using a single defect level in the band gap. We have shown that, if the level acts as a recombination center or as a majority carrier trap, the phase of the MPL depends monotonously on the frequency, and the phase diagram can be reproduced by a single arc tangent function. On the contrary, if the level acts as a minority carrier trap (its energy location being close to the minority carrier band), the phase diagram can be reproduced by a sum of three arc tangent functions defining three corner frequencies, the function with the intermediate corner frequency having an opposite sign, which thus leads to a peculiar V-shape behavior. The analytical approach has been compared to full numerical modeling, and we have studied the impacts of different parameters on the phase diagram. We have thus shown that it is possible to deduce qualitative and, to some extent, quantitative information from this experiment. This study can also point out some limitations of the low-illumination behaviour. When a single arc tangent function can fit the phase diagram, one cannot identify the origin of the recombination process (radiative or bulk SRH, or SRV). It is then mandatory to go to higher illumination intensities and to make an appropriate analysis in order to potentially distinguish between these processes. The technique could also be applied to a non homogeneous structure like a stack of semiconductor layers with different doping or a full solar cell. However, transport effects will then play

a huge role due to band bending and difference of parameters between the layers, which will then require further modeling studies in order to be able to analyze properly the experimental data.

Acknowledgement

References

[1] H.C. Casey and Frank Stern. Concentration dependent absorption and spontaneous emission of heavily doped GaAs. *Journal of Applied Physics*, 47:631–643, 1976.

[2] Wang Junling, Wu Rui, Yan Gang, and Wang Rong. Temperature-dependent photoluminescence processes of GaInP top cell irradiated with 11.5 MeV and 1.0 MeV electrons. *Nuclear Instruments & Methods in Physics Research Section B-Beam Interactions with Materials and Atoms*, 450:66–68, 2019.

[3] R.K. Ahrenkiel. Measurement of minority-carrier lifetime by time-resolved photoluminescence. *Solid-State Electronics*, 35:239–250, 1992.

[4] Matthias Maiberg and Roland Scheer. Theoretical study of time-resolved luminescence in semiconductors. I. Decay from the steady state. *Journal of Applied Physics*, 116:123710, 2014.

[5] R. Brüggemann and S. Reynolds. Modulated photoluminescence studies for lifetime determination in amorphous-silicon passivated crystalline-silicon wafers. *Journal of Non-Crystalline Solids*, 352:1888–1891, 2006.

[6] J. A. Giesecke, M. C. Schubert, and W. Warta. Self-sufficient minority carrier lifetime in silicon from quasi-steady-state photoluminescence. *physica status solidi (a)*, 209:2286–2290, 2012.

[7] Hannes Höffler, Florian Schindler, Andreas Brand, David Herrmann, Rebecca Eberle, Regina Post, Alexander Kessel, Johannes Greulich, and Martin Schubert. Review and recent development in combining photoluminescence- and electroluminescence-imaging with carrier lifetime measurements via modulated photoluminescence at variable temperatures. *37th European PV Solar and Energy Conference Exhibition*, pages 264–276, 2020.

[8] M. Pawlak. Photothermal, photocarrier, and photoluminescence phenomena in semiconductors studied using spectrally resolved modulated infrared radiometry: Physics and applications. *Journal of Applied Physics*, 126(15):150902, October 2019.

[9] I. Reklaitis, R. Kudžma, S. Miasojedovas, P. Vitta, A. Žukauskas, R. Tomašiūnas, I. Pietzonka, and M. Strassburg. Photoluminescence Decay Dynamics in Blue and Green InGaN LED Structures Revealed by the Frequency-Domain Technique. *Journal of Electronic Materials*, 45:3290–3299, 2016.

[10] I. Reklaitis, F. Nippert, R. Kudžma, T. Malinauskas, S. Karpov, I. Pietzonka, H. J. Lugauer, M. Strassburg, P. Vitta, R. Tomašiūnas, and A. Hoffmann. Differential carrier lifetime in InGaN-based light-emitting diodes obtained by small-signal frequency-domain measurements. *Journal of Applied Physics*, 121:035701, 2017.

[11] Qiming Sun, Alexander Melnikov, Andreas Mandelis, and Yaqin Song. Fully nonlinear photocarrier radiometry / modulated photoluminescence dynamics in semiconductors: Theory and applications to quantitative deconvolution of multiplexed photocarrier density wave interference and recombination processes. *Journal of Luminescence*, 236:118075, August 2021.

[12] Alexander Melnikov, Andreas Mandelis, Akshit Soral, Claudia Zavala-Lugo, and Michal Pawlak. Quantitative Imaging of Defect Distributions in CdZnTe Wafers Using Combined Deep-Level Photothermal Spectroscopy, Photocarrier Radiometry, and Lock-In Carrierography. *ACS Applied Electronic Materials*, pages 2551–2563, 2021.

[13] Baptiste Bérenguier, Nicolas Barreau, Alexandre Jaffre, Daniel Ory, Jean-François Guillemoles, Jean-Paul Kleider, and Laurent Lombez. Defects characterization in thin films photovoltaics materials by correlated high-frequency modulated and time resolved photoluminescence: An application to Cu(In,Ga)Se2. *Thin Solid Films*, 669:520–524, 2019.

[14] J. Mickevicius, G. Tamulaitis, P. Vitta, A. Zukauskas, M. S. Shur, J. Zhang, J. Yang, and R. Gaska. Carrier dynamics in GaN at extremely low excited carrier densities. *Solid State Communications*, 145(5):312–315, February 2008.

[15] Baptiste Bérenguier, Nicolas Moron, Wei Zhao, Jean Francois Guillemoles, Jean-Paul Kleider, and Laurent Lombez. High-Frequency Modulated Photoluminescence: a simulation study of cases describing the signature of carrier recombination and trap centers. In *2019 IEEE 46th Photovoltaic Specialists Conference (PVSC)*, pages 0352–0358, Chicago, IL, USA, 2019. IEEE.

[16] W. Bolton. *Control Systems*. Elsevier Science, 2002.

[17] Silvaco. Atlas user's manual, 2016.

[18] Benoit Gaury and Paul M. Haney. Probing surface recombination velocities in semiconductors using two-photon microscopy. *Journal of Applied Physics*, 119:125105, 2016.

[19] Robert Lee Chin, Michael Pollard, Thorsten Trupke, and Ziv Hameiri. Numerical simulations of two-photon absorption time-resolved photoluminescence to extract the bulk lifetime of semiconductors under varying surface recombination velocities. *Journal of Applied Physics*, 125:105703, 2019.

[20] Kai Wang and Henner Kampwerth. A Method to Separate Bulk Lifetime and Surface Recombination Velocity of Silicon Bricks based on Transient Photoluminescence. *Energy Procedia*, 55:161–168, 2014.

[21] M. Igalson and P. Zabierowski. Electron traps in Cu(In,Ga)Se2 absorbers of thin film solar cells studied by junction capacitance techniques. *Opto-electronics review*, 11:261–267, 2003.

A Appendix 1 : Corner frequencies

Demonstration that ω_1 and ω_3 are real and positive in a usual case

We define

$$\begin{cases} \omega_a = A_1 - i\omega, \\ \omega_b = -A_2, \\ \omega_c = A_3 - i\omega, \\ \omega_d = A_4 - i\omega. \end{cases} \tag{A.1}$$

First, we need to show that $\omega_0^2 \geq 0$ and $S \geq 0$. Only ω_b can be negative. If it is positive, it is straightforward. If it is negative, then we note that

$$\begin{cases} \omega_b \geq -Bn_0, \\ \omega_d \geq Bn_0, \end{cases} \tag{A.2}$$

so that

$$|\omega_b|\omega_c \leq Bn_0(v_{th}\sigma_p n_{t_0} + B(N_a + 2n_o + n_{t_0})) \leq \omega_a\omega_d. \tag{A.3}$$

So, we always have $\omega_0^2 \geq 0$ and $S \geq 0$. Consequently, we can say that if ω_1 and ω_3 are real, they are positive.

The usual case we are interested in here is the case with $\omega_c \leq \omega_a$. It is the case where more electrons occupy the defect when it is enlightened (from equation (19) $n_{t_1} \geq 0$), so when the defect is not near the valence band.

ω_1 and ω_3 are solution of

$$x^2 - S.x - \omega_0^2 = 0. \tag{A.4}$$

Let's compute the discriminant

$$\Delta = S^2 - 4\omega_0^2. \tag{A.5}$$

We have :

$$\Delta = \omega_a^2 + \omega_b^2 + \omega_d^2 + 2\omega_a\omega_b + 2\omega_a\omega_d + 2\omega_b\omega_d - 4\omega_a\omega_d - 4\omega_b\omega_c, \tag{A.6}$$

$$\Delta \geq \omega_a^2 + \omega_b^2 + \omega_d^2 + 2\omega_a\omega_b - 2\omega_a\omega_d + 2\omega_b\omega_d - 4\omega_b\omega_a, \tag{A.7}$$

$$\Delta \geq (\omega_b + \omega_d - \omega_a)^2 \geq 0, \tag{A.8}$$

so ω_1 and ω_3 are real.

Then

$$\begin{cases} \omega_1 = \dfrac{S - \sqrt{\Delta}}{2}, \\ \omega_3 = \dfrac{S + \sqrt{\Delta}}{2}. \end{cases} \tag{A.9}$$

If $\omega_b + \omega_d \geq \omega_a$

$$\begin{cases} \omega_1 \leq \dfrac{S - (\omega_b + \omega_d - \omega_a)}{2} = \omega_a, \\ \omega_3 \geq \dfrac{S + (\omega_b + \omega_d - \omega_a)}{2} = \omega_2. \end{cases} \tag{A.10}$$

If $\omega_b + \omega_d \leq \omega_a$,

$$\begin{cases} \omega_1 \leq \dfrac{S - (\omega_a - \omega_b - \omega_d)}{2} = \omega_2, \\ \omega_3 \geq \dfrac{S + (\omega_a - \omega_b - \omega_d)}{2} = \omega_a. \end{cases} \tag{A.11}$$

So, in both cases, we have $0 \leq \omega_1 \leq \omega_2 \leq \omega_3$.

B   Appendix 2 : Low-illumination approximation

We suppose we work in the low-illumination approximation, as defined in the article.

First, we will show that $\omega_{2ter}=\omega_2$.

From the hypotheses and the fact that $n_{t_1} \leq n_{t_0}$, we have

$$n_{t_1} \ll N_a + n_{t_0}. \tag{B.1}$$

In low-frequency, it can be written

$$\frac{\omega_{2bis}}{\omega_0^2}G1 \ll N_a + n_{t_0}. \tag{B.2}$$

From that, we have

$$\frac{n_0}{N_a + 2.n_0 + n_{t_0}}\frac{\omega_{2bis}}{\omega_2} \ll \frac{n_0}{N_a + 2.n_0 + n_{t_0}}\frac{\omega_0^2}{\omega_2 G_1}(N_a + n_{t_0}) \simeq \frac{G_0}{G_1} \simeq 1, \tag{B.3}$$

with, if n is a linear function of G,

$$\frac{\omega_0^2}{\omega_2 G1} = \frac{1}{n_1(\omega = 0)} \simeq \frac{G_0}{G_1 n_0}. \tag{B.4}$$

As we have

$$\omega_{2ter} = \omega_2 + \frac{n_0}{Na + 2.n_0 + n_{t_0}}\omega_{2bis}, \tag{B.5}$$

we can deduce that $\omega_{2ter}=\omega_2$.

Secondly, we need to show why we can neglect the coupling between orders 0 and 1 in the equations (17) of n_0 and n_{t_0}.

If we have $n_{t_0} \ll min(N_a, N_t)$, then :

- $2v_{th}\sigma_p n_{t_1}^2 \ll v_{th}\sigma_p n_{t_0} N_a,$

- $2Bn_1^2 \ll Bn_0 N_a,$

- $2v_{th}\sigma_p n_{t_1} n_1 cos(\phi_{n,1} - \phi_{t,1}) \ll v_{th}\sigma_p n_{t_0} N_a,$

- $2Bn_{t_1} n_1 cos(\phi_{n,1} - \phi_{t,1}) \ll Bn_0 N_a,$

- $2v_{th}\sigma_n n_{t_1} n_1 cos(\phi_{n,1} - \phi_{t,1}) \ll v_{th}\sigma_n n_0 N_t.$

If we have $n_{t_1} \ll n_{t_0}$ then :

- $2v_{th}\sigma_p n_{t_1}^2 \ll v_{th}\sigma_p n_{t_0}^2,$

- $2Bn_1^2 \ll Bn_0 N_a,$

- $2v_{th}\sigma_p n_{t_1} n_1 cos(\phi_{n,1} - \phi_{t,1}) \ll v_{th}\sigma_p n_{t_0} N_a,$

- $2Bn_{t_1} n_1 cos(\phi_{n,1} - \phi_{t,1}) \ll Bn_0 N_{t_0},$

- $2v_{th}\sigma_n n_{t_1} n_1 cos(\phi_{n,1} - \phi_{t,1}) \ll v_{th}\sigma_n n_0 N_t.$

So the system of equations (17) becomes :

$$\begin{cases} 0 = G_0 - (N_a + n_{t_0})v_{th}\sigma_p n_{t_0} - Bn_0 * (N_a + n_{t_0}) + (N_t - n_{t_0})\omega_{r,h}, \\ 0 = G_0 + n_{t_0}\omega_{r,e} - n_0 v_{th}\sigma_n(N_t - n_{t_0}) - Bn_0 * (N_a + n_{t_0}). \end{cases} \tag{B.6}$$

Consequently, n_0 and n_{t_0} are independent from n_1 and n_{t_1}.

Now, we will show some calculation steps for the approximation of the corner frequencies values in low-illumination approximation.

Trapping of electrons

As $n_{t_0} \ll N_t$, we have, from (24), that $\omega_{r,h} \ll v_{th}\sigma_p N_a$. As $E_t > E_F^*$, we have that $\omega_{r,e} \gg v_{th}\sigma_p N_a$.

Our hypotheses implies that :

- $A_1 = i\omega + v_{th}\sigma_n N_t + BN_a$

- $A_3 = i\omega + v_{th}\sigma_p n_{t_0} + BN_a$

- $A_4 = i\omega + v_{th}\sigma_p N_a + Bn_0$

- $v_{th}\sigma_n n_0 \ll \omega_{r,e} + v_{th}\sigma_p N_a$

- $v_{th}\sigma_p n_{t_0}.\omega_{r,e} \ll \omega_0^2$

- $Bn_0 v_{th}\sigma_n N_t \ll \omega_0^2$

So, from (18),

$$\begin{cases} \omega_2 = \omega_{r,e}, \\ S = \omega_{c,e} + \omega_{rad} + \omega_2, \\ \omega_0^2 = \omega_{c,e} v_{th}\sigma_p N_a + \omega_{rad}\omega_2. \end{cases} \tag{B.7}$$

Recombination center

As $n_{t_0} \ll N_t$, we have, from (24), that $\omega_{r,h} \ll v_{th}\sigma_p N_a$. As $E_t < E_F^*$, we have that $\omega_{r,e} \ll v_{th}\sigma_p N_a$.

We have the same simplifications as for the trapping of electrons.

So, we can derive from (18) :

$$\begin{cases} \omega_2 = v_{th}\sigma_p N_a, \\ S = \omega_{c,e} + \omega_{rad} + v_{th}\sigma_p N_a = \omega_2 + \omega_{c,e} + \omega_{rad}, \\ \omega_0^2 = (\omega_{c,e} + \omega_{rad})v_{th}\sigma_p N_a = \omega_2 * (\omega_{c,e} + \omega_{rad}). \end{cases} \tag{B.8}$$

Trapping of holes

We are now interested in the case of $E_t < E_F'$, with $n_{t_1} \ll n_{t_0}$. We suppose $\omega_{r,e} \ll \min(\omega_{r,h}, \omega_{c,e})$ (which is a condition very easy to meet).

Our hypotheses implies that :

- $A_1 = i\omega + v_{th}\sigma_n(N_t - n_{t_0}) + B(N_a + n_{t_0})$

- $A_3 = i\omega + v_{th}\sigma_p n_{t_0} + B(N_a + n_{t_0})$

- $A_4 = i\omega + v_{th}\sigma_p(N_a + 2n_{t_0}) + Bn_0 + \omega_{r,h}$

- $v_{th}\sigma_n n_0 \ll v_{th}\sigma_p N_a + \omega_{r,h}$

- $(v_{th}\sigma_p n_{t_0} + B(N_a + B(N_a + n_{t_0})).\omega_{r,e} \ll \omega_0^2$

- $Bn_0[v_{th}\sigma_n(N_t - n_{t_0}) - v_{th}\sigma_p n_{t_0}] \ll \omega_0^2$

- $v_{th}\sigma_n n_0 v_{th}\sigma_p n_{t_0} \ll \omega_0^2$

Then, from (18) :

$$\begin{cases} \omega_2 = \omega_{r,h} + v_{th}\sigma_p(N_a + 2n_{t_0}), \\ S = \omega_{c,e} + \omega_{rad} + \omega_{r,h} + v_{th}\sigma_p(N_a + 2n_{t_0}), \\ \omega_0^2 = (\omega_{c,e} + \omega_{rad})(\omega_{r,h} + v_{th}\sigma_p(N_a + 2n_{t_0})). \end{cases} \tag{B.9}$$